Journal of the European Ceramic Society 46 (2026) 118111

Contents lists available at ScienceDirect

Journal of the European Ceramic Society

journal homepage: www.elsevier.com/locate/jeurceramsoc

Engineering phase distribution in LSCF-CGO cathodes for enhanced electrochemical performance in SOFCs

Lucía dos Santos-Gómez [a,b,*,1], Abraham Sánchez-Caballero [a,b], José Manuel Porras-Vázquez [a,b], Javier Zamudio-García [a,b], Enrique R. Losilla [a,b], David Marrero-López [b,c,**,2]

[a] Universidad de Málaga, Departamento de Química Inorgánica, Málaga 29071, Spain
[b] Instituto Universitario de Materiales y Nanotecnología, IMANA, Málaga 29071, Spain
[c] Universidad de Málaga, Departamento de Física Aplicada I, Málaga 29071, Spain

ARTICLE INFO

Keywords:
Nanocomposite
Cathode
$La_{0.6}Sr_{0.4}Co_{0.2}Fe_{0.8}O_{3-\delta}$, $Ce_{0.9}Gd_{0.1}O_{1.95}$
Electrode morphology
SOFC

ABSTRACT

Composite cathodes combining a mixed ionic–electronic conductor with an oxygen-ion conductor are key for intermediate-temperature solid oxide fuel cells (IT-SOFCs), as they increase the electrochemically active area and mitigate thermal expansion mismatch with the electrolyte. However, conventional fabrication methods, such as simple powder mixing, often yield inhomogeneous phase distributions and involve multiple processing steps that hinder scalability. In this work, $La_{0.6}Sr_{0.4}Co_{0.2}Fe_{0.8}O_{3-\delta}$ (LSCF) - $Ce_{0.9}Gd_{0.1}O_{1.95}$ (CGO) composite cathodes are prepared by different routes, including conventional powder mixing, LSCF powders coated with CGO nanoparticles, CGO powders coated with LSCF nanoparticles and a co-synthetized nanocomposite obtained from a single precursor solution via the freeze-drying method. The electrodes are systematically characterized to correlate phase distribution and microstructure with electrochemical performance. The co-synthesized nanocomposite exhibits a significantly reduced particle size of 20 nm at 800 °C, resulting in a polarization resistance of 0.08 Ω·cm^2 at 700 °C, compared to 0.22 Ω·cm^2 for the powder-mixed electrode. Correspondingly, the power density of the cell employing the nanosized LSCF–CGO cathode increased by 37 % compared to the conventional electrode. These results demonstrate that freeze-drying provides a simple, scalable and effective synthesis route for high-performance LSCF–CGO nanocomposite cathodes, offering significant advantages over conventional preparation methods for IT-SOFC applications.

1. Introduction

Solid Oxide Fuel Cells (SOFCs) represent a promising technology for efficiently conversion of chemical energy into electricity, combining high efficiency with fuel flexibility and low emissions [1–3]. However, their widespread implementation is hindered by the need for high operating temperatures, which accelerates performance degradation. Lowering the operating temperature to the intermediate range of 650–800 °C would provide significant benefits, including the use of cost-effective materials for cell fabrication and a substantial reduction in degradation rates [4–6].

At these lower temperatures, SOFC performance is mainly limited by the sluggish oxygen reduction kinetics at the cathode [7]. The most common cathode material, $La_{0.8}Sr_{0.2}MnO_{3-\delta}$ (LSM), exhibits good electronic conductivity but acceptable oxygen reduction activity only above 800 °C [8]. Since LSM mainly acts as an electronic conductor with negligible ionic conductivity, the oxygen reduction reaction is confined to the three-phase boundary (TPB) at the electrolyte/electrode interface. Therefore, improving the catalytic activity of cathode materials is crucial to achieving high SOFC performance at reduced temperatures [9].

Alternative cobaltite-based perovskites, such as $PrBaCo_2O_{5+\delta}$ or

* Corresponding author at: Universidad de Málaga, Departamento de Química Inorgánica, Málaga 29071, Spain.
** Corresponding author at: Universidad de Málaga, Departamento de Física Aplicada I, Málaga 29071, Spain.
E-mail addresses: ldsg@uma.es (L. dos Santos-Gómez), marrero@uma.es (D. Marrero-López).
[1] Present address; Dpto. de Química Inorgánica, Cristalografía y Mineralogía, Facultad de Ciencias, Campus de Teatinos, Universidad de Málaga, 29071-Málaga, Spain
[2] Present address: Dpto. de Física Aplicada I, Facultad de Ciencias, Campus de Teatinos, Universidad de Málaga, 29071-Málaga, Spain

https://doi.org/10.1016/j.jeurceramsoc.2025.118111
Received 17 October 2025; Received in revised form 2 December 2025; Accepted 22 December 2025
Available online 23 December 2025

$Ba_{0.5}Sr_{0.5}Co_{0.8}Fe_{0.2}O_{3-\delta}$ have been investigated due to their higher ionic conductivity and enhanced electrocatalytic activity at lower temperatures. Nevertheless, these materials suffer from phase stability and high thermal expansion coefficients (TEC), which can compromise their mechanical and chemical compatibility with common electrolytes [10,11]. For this reason, $La_{0.6}Sr_{0.4}Co_{0.2}Fe_{0.8}O_{3-\delta}$ (LSCF) remains the preferred option, as it combines good catalytic activity and moderate TEC with improved chemical and mechanical stability, making it suitable for intermediate-temperature SOFCs [12,13].

Composite electrodes have been developed to further improve the chemical compatibility of LSCF and enhance its electrocatalytic performance by extending the triple-phase boundary (TPB) length for the oxygen reduction reaction (ORR) [14]. Among them, $La_{0.6}Sr_{0.4}Co_{0.2}Fe_{0.8}O_{3-\delta}$–$Ce_{0.9}Gd_{0.1}O_{1.95}$ (LSCF–CGO) composites are particularly attractive due to the strong compatibility between both phases [15]. Moreover, the morphology and particle size of the ceramic powders play a crucial role in achieving a uniform phase distribution, requiring careful control of these parameters to optimize their electrochemical performance [15–17].

The optimal LSCF content in LSCF–CGO cathodes, corresponding to the electrical percolation threshold, is typically reported between 50 and 60 wt% in LSCF [18–20]. However, the reported electrode polarization resistance of LSCF–CGO exhibits a wide variability, ranging from 0.1 to 2 $\Omega \cdot cm^2$ at 600 ºC [21–24]. Such discrepancies are generally attributed to differences in fabrication method and sintering conditions, which strongly influence the resulting electrode morphology and consequently the overall electrochemical performance [25–27].

Traditionally, these composites are fabricated by physically mixing the individual powders, a time-consuming process, as each component must first be synthesized separately and then mixed. As a result, the relatively large grain size of the starting materials makes it difficult to obtain a truly homogeneous composite with a high contact area between both phases. Although high-energy ball milling or prolonged mixing can reduce particle size and improve homogeneity, these processes may also introduce contamination from the milling media. To overcome these limitations, several alternative fabrication techniques have been explored, including infiltration, pulsed laser deposition (PLD) and spray-pyrolysis [14,28,29]. In the infiltration method, a porous CGO backbone is impregnated with an LSCF precursor solution, leading to the formation of finely distributed LSCF particles that significantly increase the active area. However, this approach typically requires multiple infiltration and calcination cycles, making the process time-consuming and difficult to reproducible. In addition, long-term stability is often limited by particle coarsening, and the scalability of the method beyond laboratory-level fabrication remains challenging [30]. PLD enables the fabrication of advanced electrodes architectures, such as vertically aligned nanocomposites (VANs) with numerous and well-controlled LSCF/CGO heterointerfaces. Nevertheless, the low porosity and limited thickness of these films, together with their high cost and poor scalability, restrict their practical application [31–34].

Hence, the preparation of composite electrodes should be simple, cost-effective, and readily scalable for industrial implementation. In this context, freeze-drying is a commercially available and well-established technique, widely used in industry for sample dehydration and easily adaptable for the synthesis of homogeneous precursor powders [35]. Moreover, its simple solvent-based processing is more compatible with large-scale or continuous manufacturing, offering clear advantages over other wet-chemical methods and making it highly suitable for large-scale SOFC electrode production. In this study, we investigate the microstructure and electrochemical properties of LSCF–CGO composites synthesized through different strategies designed to achieve a precise control over the phase distribution (Fig. 1). In the first approach, LSCF–CGO composites were prepared by the conventional mixed-powder method using commercially available powders. In the second approach, composite powders were obtained by suspending LSCF particles in a CGO nitrate precursor solution, and conversely, dispersing CGO particles in an LSCF nitrate precursor solution. After freeze-drying and calcination, this route yielded LSCF particles decorated with CGO nanoparticles and CGO particles coated with LSCF, respectively. In the third approach, LSCF–CGO nanocomposite were co-synthesized from a single precursor solution containing the required elements in stoichiometric ratios, which was freeze-dried, calcined, and

Fig. 1. Strategies used for the synthesis of the LSCF–CGO composite electrodes by the freeze-drying precursor route: (a) solution containing both LSCF and CGO phases ($LSCF_S$–CGO_S), (b) CGO solution combined with a LSCF particle suspension ($LSCF_P$–CGO_S); and (c) LSCF solution combined with a CGO particle suspension ($LSCF_P$–CGO_S).

deposited onto the electrolyte by screen-printing.

By employing different synthesis routes and electrode morphologies, we aim to clarify how variations in phase distribution affects key electrochemical parameters, such as microstructure, electrode polarization resistance, and power density in practical SOFC devices. Comprehensive microstructural and electrochemical characterization allows the identification of the most effective preparation strategy, combining enhanced electrochemical performance with simplified fabrication for the advancement of SOFC technology.

2. Experimental section

2.1. Synthesis of electrode composites

The conventional composite was prepared by mixing LSCF and CGO commercial powders (Praxair and Cerpotech, respectively) in a planetary ball milling machine (Pulverisette 7) at 200 rpm for 1.5 h.

For the one-step co-synthesized $La_{0.6}Sr_{0.4}Co_{0.2}Fe_{0.8}O_{3-\delta}$–$Ce_{0.9}Gd_{0.1}O_{1.95}$ (LSCF–CGO) nanocomposite (Fig. 1), a precursor solution was prepared by dissolving stoichiometric amounts of $Ce(NO_3)_3{\cdot}6\,H_2O$, $Gd(NO_3)_3{\cdot}6\,H_2O$, $La(NO_3)_3{\cdot}6\,H_2O$, $Sr(NO_3)_2$, $Co(NO_3)_2{\cdot}6\,H_2O$ and $Fe(NO_3)_3{\cdot}9\,H_2O$ (Merck > 99 % purity) in Milli-Q water under continuous stirring. Ethylenediaminetetraacetic acid was added as a complexing agent in a 1:1 molar ratio with respect to the total cation content. The pH was adjusted to 7 by adding an ammonia solution. The resulting solution was rapidly frozen by dropwise addition into liquid nitrogen, which was continuously stirred to prevent agglomeration of the frozen droplets. After approximately 5 min in liquid nitrogen, the frozen precursor droplets were transferred to a flask and connected to a manifold freeze-dryer (Scanvac Coolsafe). During the freeze-drying process (48 h), the condenser pressure was maintained at ~0.005 mbar and the temperature at −110 °C until complete sublimation of the frozen solvent. The resulting dried precursor was subjected to a two-stage calcination process: first at 300 ºC for 1 h to remove carbonaceous residues, and then at 800 ºC for 15 min to achieve crystallization.

The intermediate composites were prepared by combining a suspension of one oxide component in powder form with a nitrate solution of the complementary phase. Specifically, CGO suspensions were obtained by dispersing the commercial powder in Milli-Q water containing Dolapix™ (1 mL g^{-1}) as dispersant, followed by ultrasonication, and subsequently mixing with a LSCF nitrate precursor solution. Similarly, LSCF powder suspensions were prepared in the same manner and then combined with a CGO nitrate solution. In both cases, the resulting mixtures were freeze-dried and calcined at 800 ºC, as described above.

In all prepared composites, each component was fixed at 50 wt%. Hereafter, the notation $LSCF_x$–CGO_x will be used for composite electrodes, where x denotes the preparation method of each phase: freeze-dried precursor solution (S) or commercial powder (P).

2.2. Structural, microstructural and electrochemical characterization

The structural characterization of the electrodes was performed by X-ray powder diffraction (XRD) using $CuK_{\alpha1}$ radiation on a PANalytical Empyrean diffractometer. Phase identification and Rietveld refinements were carried out with the X'Pert HighScore Plus and GSAS software packages, respectively [36,37]. During the Rietveld refinement, the adjusted parameters included scale factors, background, zero shift, peak shape (modeled by pseudo-Voigt function), asymmetry, and preferential orientation. The occupancy of the cation sites was fixed and not refined.

The specific surface area of the materials was determined by N_2 adsorption. Prior to analysis, all powders were degassed at 120 °C for 12 h in a VAcPrep 0.61 unit (Micromeritics) to remove adsorbed gases and moisture. Nitrogen adsorption–desorption isotherms were recorded at −196 °C using a Micromeritics Tristar 3020 analyzer, and the specific surface area was determined using the Brunauer-Emmett-Teller (BET) method applied to the adsorption branch of the isotherm.

Microstructural analysis was performed using a field-emission scanning electron microscope (Helios Nanolab 650) equipped with an energy-dispersive X-ray spectrometer (EDS, X-Max Oxford). High-angle annular dark-field scanning transmission electron microscopy (HAADF-STEM) and high-resolution transmission electron microscopy (HRTEM) observations were conducted with a FEI Talos F200X microscope. The porosity of the electrode layers was quantified using ImageJ software by analyzing different cross-sectional SEM images.

For the electrochemical characterization, $Ce_{0.9}Gd_{0.1}O_{1.95}$ (CGO) pellets were used as electrolytes. Dense pellets were prepared by uniaxially pressing commercial CGO powders (Cerpotech) into discs of 10 mm in diameter and 1 mm in thickness, followed by sintering at 1400 ºC for 4 h, achieving a relative density above 98 %. The electrode powders were then mixed with a binder (Decoflux™), symmetrically screen-printed onto both faces of the CGO dense pellets and sintered at 1000 ºC for 1 h to ensure good adhesion to the electrolyte.

The electrode polarization resistance was evaluated by Electrochemical Impedance Spectroscopy (EIS) in a symmetrical cell configuration. A frequency response analyzer (Solartron 1260 FRA) was utilized over the frequency range of 0.01–10^6 Hz with an AC amplitude of 50 mV. Measurements were carried out under open-circuit voltage in static ambient air and as a function of the oxygen partial pressure between 450 and 750 ºC, with a stabilization time of 30 min between successive temperatures [38]. Platinum mesh and ink were used to ensure effective current collection. The individual contributions to the overall electrode polarization resistance were analyzed by equivalent circuit fitting using ZView software [39].

The performance of the composite electrodes under SOFC conditions was evaluated using anode-supported cells with a Ni-YSZ/YSZ/CGO/LSCF–CGO configuration. Commercial Ni-YSZ/YSZ anode-supported substrates (Ningbo SOFCMAN) were employed. A CGO interlayer was introduced between the electrolyte and the cathode by screen-printing, followed by sintering at 1100 ºC for 1 h to suppress detrimental reactions between YSZ and LSCF [40,41]. The LSCF–CGO composite cathode was subsequently deposited by screen-printing method and sintered under the same conditions [42]. The assembled cells were sealed to an alumina tube using a ceramic adhesive (Ceramabond 668, Aremco). Current–voltage curves and impedance spectra were recorded with a Zahner Zennium XC in the temperature range 800–650 ºC, using humidified hydrogen (3 vol.% H_2O) as the fuel and static air as the oxidant.

3. Results and discussion

3.1. Structural characterization of the materials

The XRD patterns of the four LSCF–CGO composite electrodes calcined at 800 ºC are shown in Fig. 2a. Diffraction peaks corresponding to the perovskite LSCF and fluorite CGO phases are clearly identified, confirming the formation of the expected crystal structures without detectable secondary phases. Variations in the relative peak intensities are observed among the patterns, which can be attributed to microstructural differences arising from the synthesis, such as particle size, degree of agglomeration and crystallite orientation. Since these effects influence the diffraction response in different ways, no consistent trend is observed across the samples.

Rietveld refinements of the XRD data were performed assuming the cubic $Fm\bar{3}m$ and rhombohedral $R\bar{3}c$ space groups for CGO and LSCF, respectively. Fig. 2b shows the refinement of the $LSCF_S$–CGO_S nanocomposite as a representative example, and the refined parameters are summarized in Table 1. The disagreement factors between the observed and calculated patterns were satisfactory, with R_{wp} values below 2.66 %. The phase composition determined from the refinement was consistent with the nominal values, remaining close to 50 wt% for each phase (Table 1).

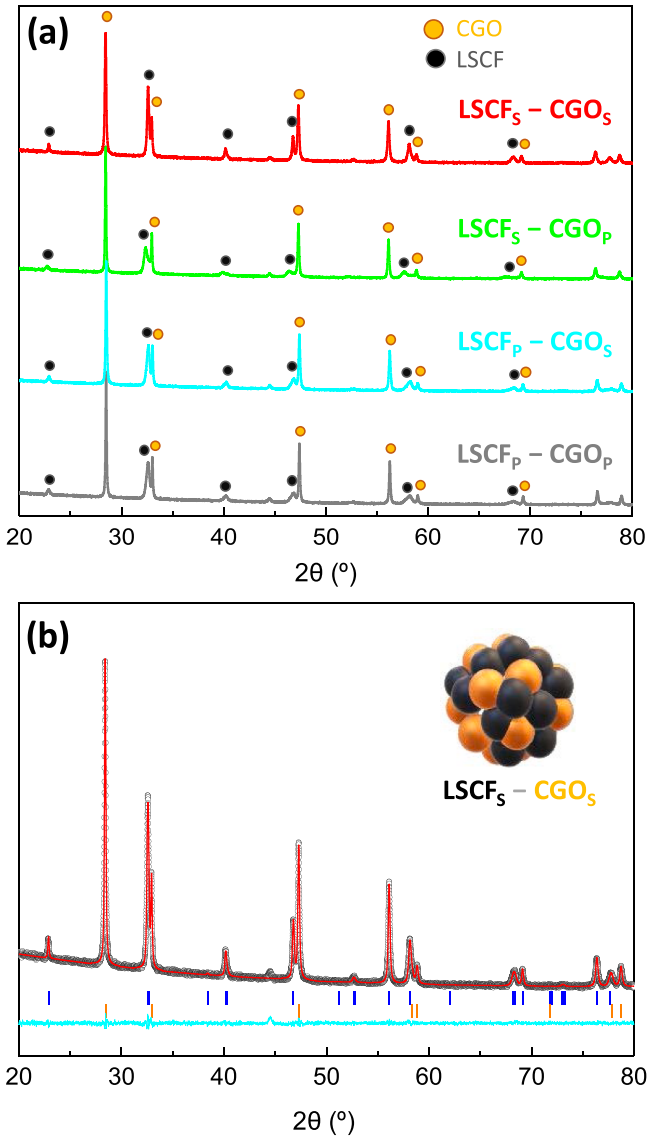

Fig. 2. XRD patterns of the LSCF-CGO composite electrodes calcined at 800 °C and obtained from the different synthetic strategies.

The evolution of the lattice parameters and the phase quantification confirm that the CGO and LSCF phases obtained in the different composites maintain essentially the same compositions and cell parameters as the reference powders. Moreover, any minor cation intermixing that may occur during the co-synthesis process does not affect the electrochemical properties, as no secondary phases are detected. On the contrary, Co incorporation into the CGO lattice has been reported to enhance its electronic conductivity, which could be beneficial for the performance of composite cathodes [43].

3.2. Microstructural characterization

Fig. 3 shows HAADF-STEM images with the corresponding elemental mappings of the composites prepared by different synthetic approaches and calcined at 800 °C. These strategies were designed to produce composite powders with different phase distributions, as previously described and illustrated in Fig. 1.

In the LSCF$_S$–CGO$_S$ composite, large CGO particles (~ 400 nm) are decorated with smaller LSCF nanoparticles (Fig. 3a). Elemental mapping reveals a uniform distribution of Fe across the particle surface, while Ce is concentrated in the inner regions, confirming a homogeneous LSCF coating (Fig. 3b-d). This configuration ensures good interfacial contact, which may favor electronic conduction at the electrode surface. In contrast, the LSCF$_P$–CGO$_S$ nanocomposite shows the opposite arrangement: larger LSCF particles (>500 nm) from the commercial powder are coated with nanosized CGO nanoparticles (Fig. 3e). The EDS maps reveal that CGO forms a thin and continuous layer over the LSCF grains (Fig. 3f-h), creating an extended interfacial area that provides preferred ionic conduction pathways at the electrode surface, although the electronic conduction may be partially hindered by the predominately ionic nature of CGO coating.

The co-synthesized LSCF$_S$–CGO$_S$ nanocomposite (Fig. 3i) displays a drastically reduced particle size (~15 nm) and a highly homogeneous phase distribution (Fig. 3j-l), demonstrating the effectiveness of the freeze-drying approach in producing finely intermixed, self-assembled nanocomposites. The intimate nanoscale mixing suppresses grain coarsening during calcination, as each particle is surrounded by a phase of different composition. Similar behavior has been reported for other self-assembled nanocomposite electrodes, such as $Sr_{0.5}Sm_{0.5}CoO_3$–$Ce_{0.8}Sm_{0.2}O_{1.9}$ or $La_{0.8}Sr_{0.2}MnO_3$-$Ce_{0.8}Gd_{0.2}O_{1.9}$ [45], where the extended TPB facilitates simultaneous electron and oxide-ion transport across the electrode surface.

The BET surface area values of the electrodes range from 7 $m^2\ g^{-1}$ for LSCF$_P$–CGO$_P$ to 18 $m^2\ g^{-1}$ for LSCF$_S$–CGO$_S$ (Table 1). Although the co-synthesized LSCF$_S$-CGO$_S$ sample exhibits the highest value, the differences among the samples remain small, which is expected given that all powders were calcined at the relatively high temperature of 800 °C.

HRTEM images corroborate these findings. In the LSCF$_P$–CGO$_S$ composite, the commercial LSCF grains are coated with CGO nanoparticles of ~20 nm in diameter (Fig. 4a). The corresponding SAED pattern (Fig. 4b) shows diffuse concentric rings characteristic of a polycrystalline material, which can be indexed to the cubic fluorite of CGO, with d-spacings in very good agreement with those obtained from XRD. Reflections from LSCF are not observed in the SAED pattern because the LSCF grains are significantly larger, leading to a limited number of diffracting domains and consequently negligible diffraction intensity. These results demonstrate that CGO nanoparticles nucleate and grow uniformly on the LSCF surface, generating an intimate contact between both phases and ensuring a large interfacial area.

In contrast, the LSCF$_S$–CGO$_P$ composite exhibits large CGO grains coated with LSCF nanoparticles (Fig. 4c). The morphological differences with respect to LSCF$_P$–CGO$_S$ sample can be directly attributed to the nature of the precursor solution, which governs the growth kinetics. In particular, the presence of cobalt in the precursor solution enhances

Table 1
Composite abbreviations, source of each component (powder or solution), structural parameters and BET surface area of the as-prepared powders at 800 °C.

Abbreviation	Source	a(Å)	c(Å)	V/Z(Å^3)	weight(%)	R_{wp}(%)	R_F (%)	S_{BET} ($m^2\ g^{-1}$)
LSCF$_P$	Powder	5.4935(2)	13.4268(2)	58.49(1)	52.0(1)	2.37	2.58	7
CGO$_P$	Powder	5.4204(1)	-	39.81(1)	48.0(1)		0.56	
LSCF$_S$	Solution	5.4959(1)	13.4107(1)	58.47(1)	50.7(1)	2.25	2.78	18
CGO$_S$	Solution	5.4317(1)	-	40.06(1)	49.3(1)		0.46	
LSCF$_P$	Powder	5.4890(2)	13.4260(1)	58.52(1)	51.2(1)	2.35	3.39	10
CGO$_S$	Solution	5.4226(1)	-	39.86(1)	48.8(1)		0.65	
LSCF$_S$	Solution	5.5358(2)	13.3930(1)	59.24(1)	52.8(1)	2.66	2.95	12
CGO$_P$	Powder	5.4308(1)	-	40.04(1)	47.2(1)		1.71	

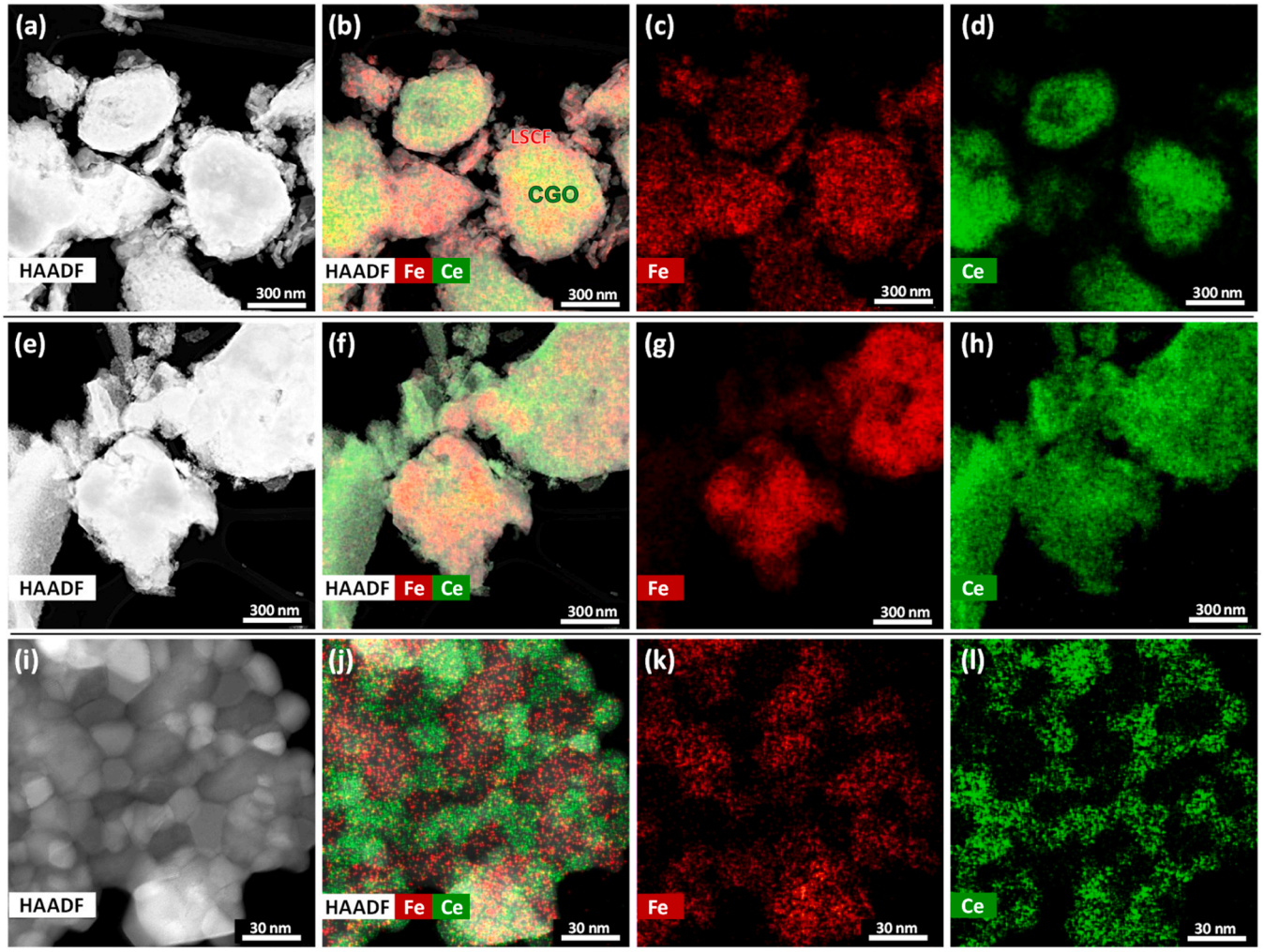

Fig. 3. HAADF images and elemental distribution of representative elements (Ce and Fe) of the as-synthesized composite powders at 800 ºC: (a-d) LSCF solution combined with a CGO particle suspension ($LSCF_S$–CGO_P); (e-h) freeze-drying of a CGO solution combined with an LSCF particle suspension ($LSCF_P$–CGO_S) and (i-l) freeze-drying of co-sintered LSCF–CGO solutions ($LSCF_S$–CGO_S).

densification and accelerates the grain growth of LSCF, promoting the formation of larger and more irregular LSCF particles at low sintering temperatures. As a result, the interfacial area between LSCF and CGO is reduced, which may compromise the connectivity of triple-phase boundaries and limit the efficiency of ionic-electronic transport across the composite electrode.

After calcination at 800 ºC, the $LSCF_S$–CGO_S composite retains its nanostructured architecture consisting of highly crystalline particles with an average diameter of 20 nm (Fig. 4d). The corresponding SAED pattern (Fig. 4e) shows reflections from both the cubic CGO and rhombohedral LSCF, confirming the coexistence of the two homogeneously distributed crystalline phases. HRTEM images at higher magnification (Fig. 4f) further reveal the intimate mixture of LSCF and CGO nanoparticles, with well-defined lattice fringes corresponding to different crystallographic planes of both phases. The measured D-spacings (d_{111} ~ 3.2 Å and d_{200} ~ 5.5 Å for CGO; d_{100} ~5.6 Å and d_{001}~13.3 Å for LSCF) are fully consistent with the crystal structures determined by XRD.

Cross-sectional SEM images of the symmetrical cells sintered at 1000 ºC for 1 h show a similar electrode thickness of approximately 20 μm and good adhesion to the electrolyte in all cases, ensuring efficient ionic transport across the electrode/electrolyte interface (Fig. 5). All electrodes display interconnected porosity; however, the degree of porosity and phase connectivity between LSCF and CGO depend on the preparation route. Regarding the porosity, all electrodes exhibit comparable values in the range 38–42 %. However, notable differences in pore distribution are observed. In particular, the $LSCF_S$–CGO_P electrode shows a heterogeneous porosity, with regions containing larger pores mixed alongside denser areas. In contrast, $LSCF_S$–CGO_S electrode exhibits a much more homogeneous porosity (Fig. 5d).

EDS elemental mapping demonstrates that, regardless of the route employed, the two phases are generally well distributed across the cathode thickness, with the exception of the mixed-powder composite, where regions enriched in either CGO or LSCF are evident (Fig. 5a), highlighting the limited homogeneity of this approach. In contrast, the freeze-drying routes produce finer and more uniform phase distributions, generating extended nanoscale contact points between the electronic and ionic conducting phases. Such intimate mixing is expected to enhance electrochemical activity by reducing electrode polarization losses. Among the different routes, the co-synthesized $LSCF_S$–CGO_S exhibits the most uniform and finely distributed microstructure, whereas in the $LSCF_S$–CGO_P, the LSCF component tends to concentrate near the electrode surface, as expected (Fig. 5c).

The structural and microstructural features of the LSCF–CGO composites indicate that these electrodes are expected to exhibit good electrochemical performance and stability under intermediate-temperature SOFC operation. The chemical compatibility between LSCF and CGO, together with their similar thermal expansion

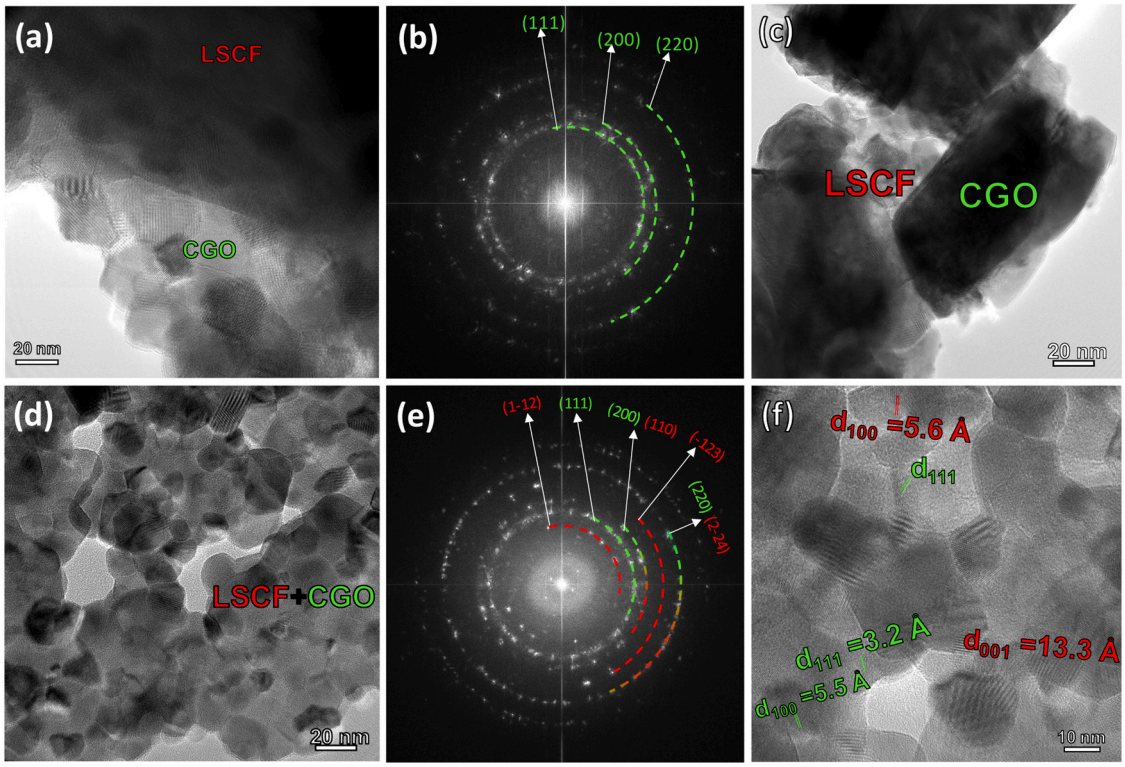

Fig. 4. (a) HRTEM image of $LSCF_P$–CGO_S showing large LSCF particles coated with CGO nanoparticles, and the corresponding (b) SAED pattern. (c) HRTEM image of $LSCF_S$–CGO_P. (d) HRTEM image of $LSCF_S$–CGO_S showing a homogeneous distribution of both phases, with the corresponding (e) SAED pattern and (f) high magnification HRTEM highlighting the D-spacing of the phase components.

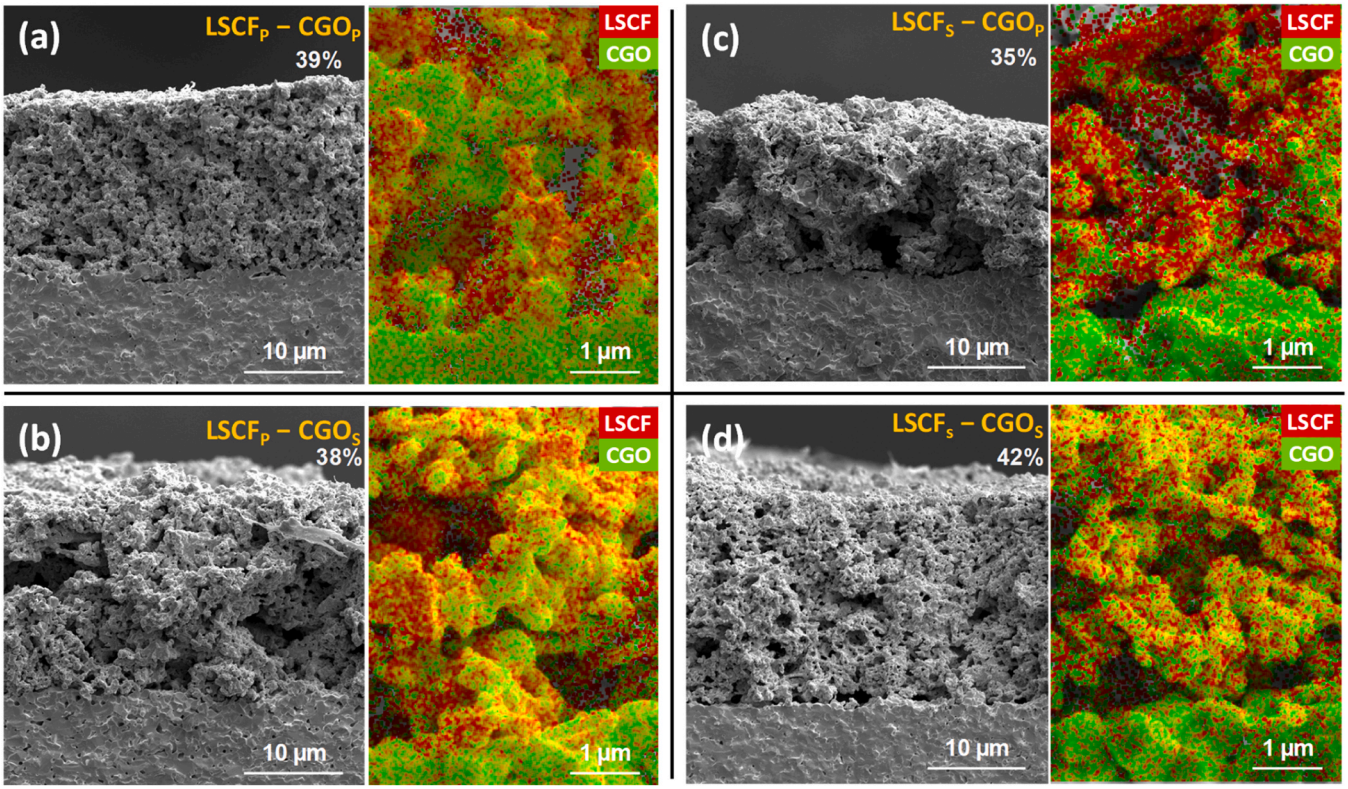

Fig. 5. Cross-sectional SEM image and corresponding EDS elemental maps of the different symmetrical cells with different electrodes: (a) $LSCF_P$–CGO_P, (b) $LSCF_S$–CGO_P, (c) $LSCF_P$–CGO_S and (d) $LSCF_S$–CGO_S. The estimated porosity values of the electrodes are indicated in each figure.

coefficients (≈13–15 × 10^{-6} K^{-1}), minimizes thermo-mechanical stresses during thermal cycling. In this context, previous studies have

reported stable polarization resistance up to 700–800 °C [44], and the preserved microstructure after operation in this work further supports the expected stability of these electrodes.

3.3. Electrochemical characterization

Impedance spectra at 600 °C in air are compared in Fig. 6a. Although the overall shape of the spectra is similar for all electrodes, both the total electrode polarization resistance and the ohmic resistance vary depending on the electrode configuration. The impedance data were satisfactorily fitted using an equivalent circuit consisting of two main contributions, represented by two RQ elements connected in series, together with a series resistance (R_s) associated with the ohmic losses of the electrolyte and electrodes, and an inductive element (L) accounting for the contribution of the measurement setup (inset Fig. 6a). The processes appear at practically the same characteristic frequencies for the different electrodes: ~10^4 Hz for the high-frequency (HF) contribution and 10–100 Hz for the low-frequency (LF) contribution, indicating that similar electrochemical processes are involved in the different electrode configurations.

The impedance spectra were also collected as a function of the oxygen partial pressure (pO_2) for the $LSCF_S$–CGO_S electrode (Fig. 6b) to determine the dependence of the different electrode contributions, which typically follow a relationship of $R \sim (pO_2)^{-m}$ where the exponent m allows the identification of the rate-limiting steps of the oxygen reduction reaction [27]. The HF contribution is nearly independent of pO_2, with m= 0.02 (Fig. 6c), indicating that this process is associated with oxide-ion transfer across the electrode/electrolyte interface ($O^x_{O,electrode} \rightarrow O^x_{O,electrolyte}$) [27]. This process is relatively small for the $LSCF_S$–CGO_S nanocomposite cathode due to the enhanced ionic transport at the electrolyte interface. In contrast, the LF process is dominant, exhibiting m= 0.27, close to the theoretical value of 0.25, which is consistent with a charge-transfer step on the electrode surface: $O_{ad} + 2e' + V_{\ddot{O}} \rightarrow O^x_O$. Similar rate-limiting steps have been reported for nanostructured LSCF electrodes [20].

The temperature dependence of the electrode polarization resistance (R_p) demonstrates that the $LSCF_S$–CGO_S nanocomposite exhibits the lowest R_p within the studied temperature range, reaching 0.08 Ω·cm^2 at 700 °C (Fig. 6d). This value is significantly lower than that obtained for the traditional mixed-powder composite $LSCF_P$–CGO_P (0.22 Ω·cm^2). In contrast, the composite electrodes formed by coated-powder phases ($LSCF_S$–CGO_P and $LSCF_P$–CGO_S) do not show substantial improvement, presenting R_p values of about 0.14 and 0.18 Ω·cm^2, respectively. Reported R_p values in the literature (Table 2) cover a wide range, extending from 0.2 to 0.3 Ω·cm^2 for powder-mixed electrodes [46,47], ~0.05–0.2 Ω·cm^2 for infiltrated electrodes [48,49], and ~0.04 Ω·cm^2 for spray-pyrolyzed electrodes [20]. The activation energies of R_p determined for the different electrode configurations fall within a narrow range of 1.18–1.21 eV, which is comparable to values reported in the literature [50,51]. Although infiltrated and spray-pyrolyzed electrodes generally exhibit lower R_p values due to their fine microstructure and high active surface area, their fabrication is limited to relatively low temperatures, which raises concerns about long-term stability associated with grain growth and coarsening. In contrast, traditional composite electrodes prepared by powder mixing show significantly higher R_p values, confirming the benefit of the freeze-drying approach in achieving better phase dispersion and enhanced electrode performance. These results highlight the advantages of the freeze-drying synthesis

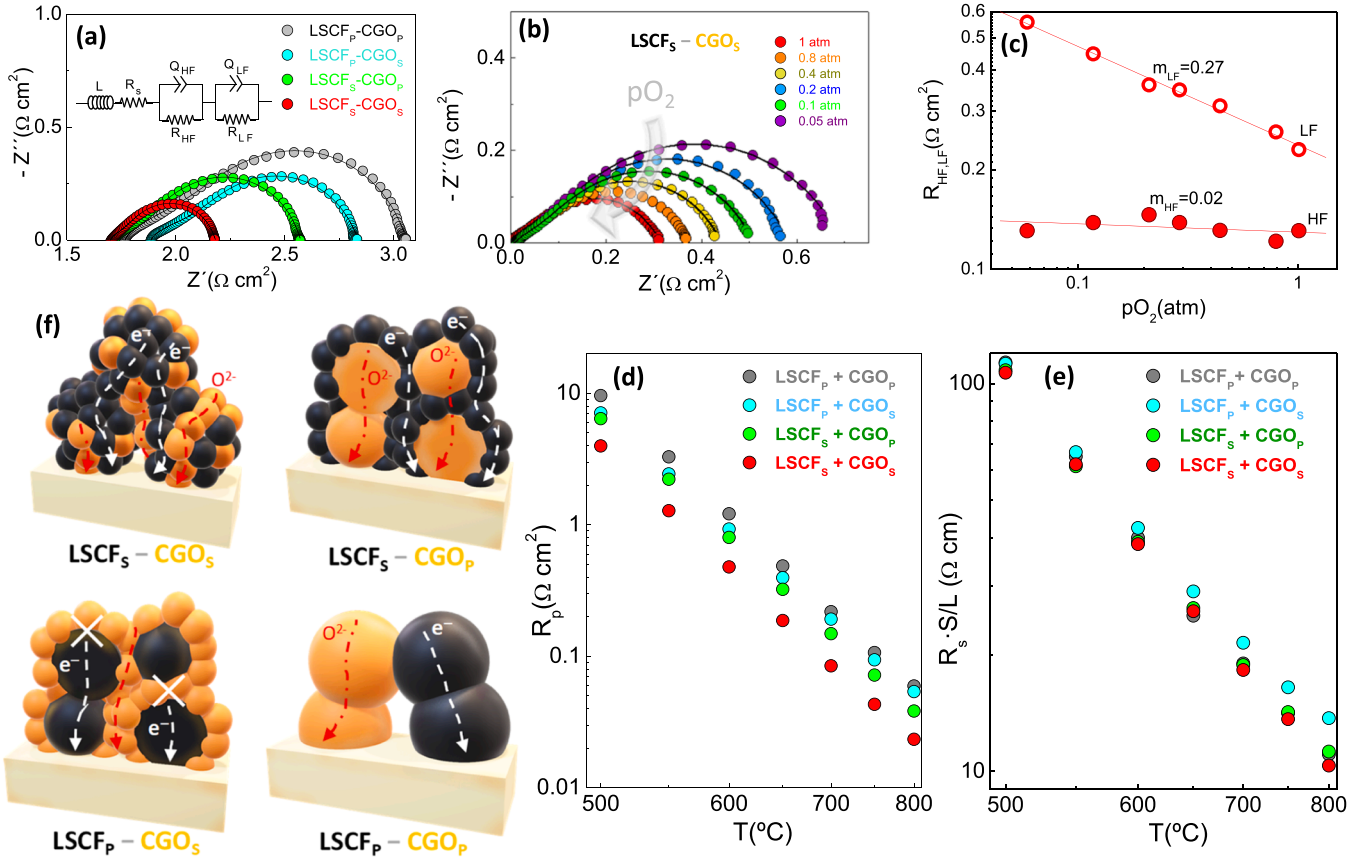

Fig. 6. (a) Impedance spectra of the different LSCF–CGO composite electrodes in air at 600 °C. (b) Impedance spectra of $LSCF_S$–CGO_S electrode recorded at different pO_2 values at 600 °C, and (c) the corresponding pO_2 dependence of the electrode contributions. Temperature dependence of the (d) electrode polarization resistance and (e) ohmic resistance of the symmetrical cells. (f) Schematic representation of the ionic and electronic conduction pathways in the different composite electrodes. The equivalent circuit used for impedance fitting is shown in the inset of (a).

Table 2
Synthetic conditions and electrode polarization resistance (R_p) of $La_{0.6}Sr_{0.4}Fe_{0.8}Co_{0.2}O_{3-\delta}$ (LSCF)-based composites electrodes reported in literature. R_p values are given at 700 ºC. For cases where data are not available at 700 °C, the corresponding measurement temperature is indicated.

Composition	Preparation Technique	Sintering Temperature	R_p ($\Omega \cdot cm^2$)	Ref
$LSCF_P$–CGO_P	Freeze-drying	1000 ºC, 1 h	0.22	This work
$LSCF_P$–CGO_S	Freeze-drying	1000 ºC, 1 h	0.19	This work
$LSCF_S$–CGO_P	Freeze-drying	1000 ºC, 1 h	0.15	This work
$LSCF_S$–CGO_S	Freeze-drying	1000 ºC, 1 h	0.08	This work
LSCF–$Ce_{0.9}Gd_{0.1}O_{1.95}$	Electrostatic Spray Deposition	900 ºC, 2 h	0.20	[52]
LSCF–$Ce_{0.9}Gd_{0.1}O_{1.95}$	Spray-pyrolysis	650 ºC, 2 h	0.04	[20]
LSCF–$Ce_{0.8}Gd_{0.2}O_{1.9}$	Inkjet printing	1150 ºC, 2 h	$0.62^{650\ ºC}$	[53]
LSCF–$Ce_{0.8}Gd_{0.2}O_{1.9}$	Spray-coating	1000 ºC, 2 h	0.13	[46]
LSCF–$Ce_{0.8}Gd_{0.2}O_{1.9}$	Bilayer, Spray-pyrolysis	650 ºC, 4 h	$0.7^{650\ ºC}$	[54]
LSCF–$Ce_{0.8}Gd_{0.2}O_{1.9}$	Spray-pyrolysis	700 ºC, 4 h	$3.0^{600\ ºC}$	[25]
LSCF–$Ce_{0.8}Gd_{0.2}O_{1.9}$	Electrospinning+Infiltration	800 ºC, 1 h	0.14	[55]
LSCF–$Ce_{0.8}Gd_{0.2}O_{1.9}$	Infiltration	800 ºC, 1 h	0.04	[49]
LSCF–$Ce_{0.8}Sm_{0.2}O_{1.9}$	Co-precipitation+Screen-printing	1100 ºC, 2 h	0.23	[56]
LSCF–$Ce_{0.8}Sm_{0.2}O_{1.9}$	Infiltration (CGO)	900 ºC,1 h	0.17	[48]
LSCF–$Ce_{0.8}Sm_{0.2}O_{1.9}$	Microwave combustion	1150 ºC, 4 h	$2.77^{800\ ºC}$	[57]
LSCF–$Er_{0.4}Bi_{1.6}O_3$	Traditional composite	800 ºC, 2 h	$0.38^{600\ ºC}$	[47]
LSCF–$Er_{0.4}Bi_{1.6}O_3$	Infiltration	1080 ºC, 2 h	0.11	[58]
LSCF–$Y_{0.5}Bi_{1.5}O_3$	Infiltration	1000 ºC, 3 h	$11.40^{500\ ºC}$	[59]

route employed in this work.

Another important difference among the electrode configurations concerns the ohmic resistance of the cells (R_s), which varies significantly depending on the phase distribution within the composite electrodes (Fig. 6e). The lowest series resistance values are obtained for the mixed-powder and co-synthesized electrodes, whereas the $LSCF_P$–CGO_S electrode exhibits higher R_s values, particularly at elevated temperatures. A schematic illustration for such findings, as well as of the improved performance of the $LSCF_S$–CGO_S electrode, is shown in Fig. 6f. The nanocomposite electrode, with its intimate mixture of nanosized particles, provides numerous electronic and ionic conduction pathways extending to the electrode surface, in contrast to the more limited connectivity of the large particles within the powder-mixed electrode. This effectively extends the TPB length, leading to a significant reduction in R_p. In contrast, for the $LSCF_S$–CGO_P, the large CGO particle size combined with the coarsening of the coated LSCF particles at high sintering temperatures reduces both porosity and TPB density, resulting in larger R_p values. Finally, in the case of $LSCF_P$–CGO_S, the preferential distribution of CGO on the electrode surface blocks the electronic conduction, as evidenced by the marked increase in the ohmic resistance of the cells. Consequently, no significant improvement in R_p is achieved for this configuration.

Fuel cell tests were carried out for $LSCF_P$–CGO_P and $LSCF_S$–CGO_S cathodes using commercial NiO-YSZ/YSZ anode-supported cells, ensuring that the observed differences in efficiency can be attributed exclusively to the cathode. The open circuit voltages (OCV) of the cells are similar and close the theoretical Nernst potential (~1.1 V) for 97 % H_2 + 3 % H_2O as fuel and air as oxidant, confirming adequate sealing in both cells (Figs. 7a and 7b). The maximum power density for the cell with $LSCF_P$–CGO_P cathode is 0.8 $W \cdot cm^{-2}$ at 800 ºC, whereas the nanocomposite $LSCF_S$–CGO_S electrode delivers 1.1 $W \cdot cm^{-2}$ at the same temperature, corresponding to a 37 % increase in power density. The I–V curves are nearly linear over the current density range studied, indicating that the cell performance is primarily governed by ohmic resistance.

These values of power density are competitive with those reported in literature for NiO-YSZ/YSZ anode-supported cells with LSCF-based cathodes, such as screen-printed LSCF–CSO (0.65 $W \cdot cm^{-2}$ at 750 ºC) [60], honeycomb-shaped LSCF–CGO (0.48 $W \cdot cm^{-2}$ at 750 ºC) [61] and infiltrated LSCF–ESB (0.47 $W \cdot cm^{-2}$ at 700 ºC) [58]. Further enhancement in power density can be achieved by reducing the thickness of the YSZ electrolyte, thereby minimizing the ohmic resistance and enabling higher current densities at intermediate temperatures.

The cross-sectional SEM image of the cell with the $LSCF_S$–CGO_S cathode after the electrochemical characterization is shown in Fig. 7c. The microstructure reveals well-defined interfaces and good adhesion between the different layers, with thicknesses of approximately 8 μm for the YSZ electrolyte and 3 μm for the CGO interlayer. No appreciable cation interdiffusion is observed across the cell layers, confirming its chemical stability. The cathode exhibits a highly porous microstructure, which ensures efficient gas diffusion and a high TPB density for electrochemical reactions.

4. Conclusions

LSCF–CGO composite electrodes for SOFCs were synthesized through different routes to tailor the phase distribution, including conventional powder mixing, combinations of powder suspensions and

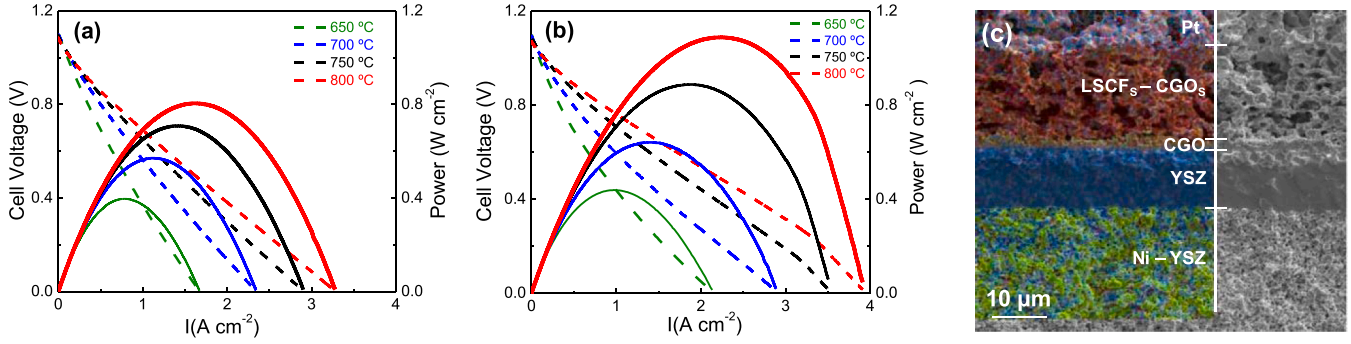

Fig. 7. Cell voltage and power density curves of Ni-YSZ/YSZ/CGO cells with composite cathodes of (a) $LSCF_P$–CGO_P and (b) $LSCF_S$–CGO_S. (c) Cross-sectional SEM image of the cell with the $LSCF_S$-CGO_S cathode.

nitrate solutions to obtain coated powders, and a one-step freeze-drying precursor method from a single precursor solution. Structural analysis by XRD and HRTEM confirmed the coexistence of perovskite LSCF and fluorite CGO phases, with phase fractions close to the nominal values. The co-synthesized electrodes exhibited a homogeneous phase distribution with an average particle diameter of 20 nm, thereby promoting extended triple-phase boundaries for the electrochemical reaction. The coated-powder routes also demonstrated improved nanoscale contact between the electronic and ionic conducting phases compared with conventional mixed powder approach.

Electrochemical impedance spectroscopy further confirmed that the freeze-dried and coated-powder composites exhibited lower polarization resistance than the conventional mixed-powder electrodes, in direct correlation with their improved microstructural features. In particular, R_p values decreased from 0.22 Ω·cm^2 at 700 ºC for the mixed-powder electrode to 0.08 Ω·cm^2 for the co-synthesized nanocomposite. In addition, NiO-YSZ/YSZ anode-supported single cells delivered power densities of 0.8 W·cm^{-2} for the conventional electrode and 1.1 W·cm^{-2} for the nanocomposite cathode. These results highlight the critical role of phase distribution in achieving not only lower electrode polarization resistance but also reduced ohmic losses. Overall, the freeze-drying method emerges as a simple, reproducible, and scalable strategy for producing highly active nanocomposite cathodes, thereby contributing to the development and commercialization of next-generation SOFC technology. Future work should focus on investigating scale-up effects on powder homogeneity and microstructure, as well as evaluating process efficiency and cost when applied to large-volume production.

CRediT authorship contribution statement

Lucía dos Santos-Gómez: Writing – original draft, Visualization, Methodology, Investigation, Data curation, Conceptualization. **Abraham Sánchez-Caballero:** Validation, Methodology, Investigation. **David Marrero-López:** Supervision, Project administration, Investigation, Funding acquisition, Formal analysis, Conceptualization. **José Manuel Porras-Vázquez:** Funding acquisition, Formal analysis. **Javier Zamudio-García:** Validation, Methodology, Investigation. **Enrique R. Losilla:** Supervision, Project administration.

Declaration of Competing Interest

The authors declare that they have no known competing financial interests or personal relationships that could have appeared to influence the work reported in this paper.

Acknowledgements

This work was supported by project PID2024–157418OB-I00, funded by MCIN/AEI/10.13039/501100011033 Spain and co-financed in by the European Union through “ERDF A way of making Europe”, as well as by project DGP_PIDI_2024_00032 from the Junta de Andalucía. LdSG gratefully acknowledge the Universidad de Málaga for the funding through the JA.B1–20 project.

References

[1] M. Singh, D. Zappa, E. Comini, Solid oxide fuel cell: decade of progress, future perspectives and challenges, Int. J. Hydrog. Energy 46 (2021) 27643–27674.
[2] X. Lu, W. Gang, Z. Tu, Recent developments in control and integration of solid oxide fuel cells: From stack to system, Renew. Sustain. Energy Rev. 223 (2025) 116000.
[3] M. Yousaf, Y. Lu, M. Akbar, L. Lei, S. Jing, Y. Tao, Advances in solid oxide fuel cell technologies: lowering the operating temperatures through material innovations, Mater. Today Energy 44 (2024) 101633.
[4] Y. Zhang, R. Knibbe, J. Sunarso, Y. Zhong, W. Zhou, Z. Shao, Z. Zhu, Recent progress on advanced materials for solid-oxide fuel cells operating below 500 °C, Adv. Mater. 29 (2017) 1700132.
[5] N. Shaheen, Z. Chen, Y. Nong, T. Su, M. Yousaf, M. Alomar, Y. Lu, Progress in nanotechnology development and nano-material selection for low-temperature solid oxide fuel cell, J. Alloy. Compd. 977 (2024) 173212.
[6] Z. Gao, L.V. Mogni, E.C. Miller, J.G. Railsback, S.A. Barnett, A perspective on low-temperature solid oxide fuel cells, Energy Environ. Sci. 9 (2016) 1602–1644.
[7] N.N.M. Tahir, N.A. Baharuddin, A.A. Samat, N. Osman, M.R. Somalu, A review on cathode materials for conventional and proton-conducting solid oxide fuel cells, J. Alloy. Compd. 894 (2022) 162458.
[8] S.P. Jiang, Development of lanthanum strontium manganite perovskite cathode materials of solid oxide fuel cells: a review, J. Mater. Sci. 43 (2008) 6799–6833.
[9] E.A. Kotomin, Y.A. Mastrikov, R. Merkle, J. Maier, First principles calculations of oxygen reduction reaction at fuel cell cathodes, Curr. Opin. Electrochem. 19 (2020) 122–128.
[10] Y. Wan, Y. Xing, Y. Li, D. Huan, C. Xia, Thermal cycling durability improved by doping fluorine to $PrBaCo_2O_{5+\delta}$ as oxygen reduction reaction electrocatalyst in intermediate-temperature solid oxide fuel cells, J. Power Sources 402 (2018) 363–372.
[11] B. Wei, Z. Lü, X. Huang, J. Miao, X. Sha, X. Xin, W. Su, Crystal structure, thermal expansion and electrical conductivity of perovskite oxides $Ba_xSr_{1-x}Co_{0.8}Fe_{0.2}O_{3-\delta}$ ($0.3\leq x\leq 0.7$), J. Eur. Ceram. Soc. 26 (2006) 2827–2832.
[12] R. Vinoth Kumar, A.P. Khandale, A review on recent progress and selection of cobalt-based cathode materials for low temperature-solid oxide fuel cells, Renew. Sustain. Energy Rev. 156 (2022) 111985.
[13] S.P. Jiang, Development of lanthanum strontium cobalt ferrite perovskite electrodes of solid oxide fuel cells – A review, Int. J. Hydrog. Energy 44 (2019) 7448–7493.
[14] A.M. Mehdi, A. Hussain, R.H. Song, T.-H. Lim, W.W. Kazmi, H.A. Ishfaq, M. Z. Khan, S. Qamar, M.W. Syed, M.T. Mehran, Improving the durability of cobaltite cathode of solid oxide fuel cells – a review, RSC Adv. 13 (2023) 25029–25053.
[15] A.K. Yadav, S. Sinha, A. Kumar, Advancements in composite cathodes for intermediate-temperature solid oxide fuel cells: a comprehensive review, Int. J. Hydrog. Energy 59 (2024) 1080–1093.
[16] E. Filonova, E. Pikalova, Overview of approaches to increase the electrochemical activity of conventional perovskite air electrodes, Materials (2023).
[17] A.J. Abd Aziz, N.A. Baharuddin, M.R. Somalu, A. Muchtar, Review of composite cathodes for intermediate-temperature solid oxide fuel cell applications, Ceram. Int. 46 (2020) 23314–23325.
[18] Y.T. Kim, A. Ohi, A. He, Z. Jiao, T. Shimura, D. Klotz, S. Hara, N. Shikazono, Microstructure and polarization characteristics of LSCF-GDC composite cathode with different volume fractions, ECS Trans. 68 (2015) 757.
[19] M.J. López-Robledo, M.A. Laguna-Bercero, J. Silva, V.M. Orera, A. Larrea, Electrochemical performance of intermediate temperature micro-tubular solid oxide fuel cells using porous ceria barrier layers, Ceram. Int. 41 (2015) 7651–7660.
[20] L. dos Santos-Gómez, J.M. Porras-Vázquez, E.R. Losilla, F. Martín, J.R. Ramos-Barrado, D. Marrero-López, LSCF-CGO nanocomposite cathodes deposited in a single step by spray-pyrolysis, J. Eur. Ceram. Soc. 38 (2018) 1647–1653.
[21] Ö Çelikbilek, E. Siebert, D. Jauffrès, C.L. Martin, E. Djurado, Influence of sintering temperature on morphology and electrochemical performance of LSCF/GDC composite films as efficient cathode for SOFC, Electrochim. Acta 246 (2017) 1248–1258.
[22] J. Nielsen, T. Jacobsen, M. Wandel, Impedance of porous IT-SOFC LSCF:CGO composite cathodes, Electrochim. Acta 56 (2011) 7963–7974.
[23] M.J. López-Robledo, M.A. Laguna-Bercero, A. Larrea, V.M. Orera, Reversible operation of microtubular solid oxide cells using $La_{0.6}Sr_{0.4}Co_{0.2}Fe_{0.8}O_{3-\delta}$-$Ce_{0.9}Gd_{0.1}O_{2-\delta}$ oxygen electrodes, J. Power Sources 378 (2018) 184–189.
[24] J. Sar, F. Charlot, A. Almeida, L. Dessemond, E. Djurado, Coral microstructure of graded CGO/LSCF oxygen electrode by electrostatic spray deposition for energy (IT-SOFC, SOEC), Fuel Cells 14 (2014) 357–363.
[25] B.F. Angoua, E.B. Slamovich, Single solution spray pyrolysis of $La_{0.6}Sr_{0.4}Co_{0.2}Fe_{0.8}O_{3-\delta}$–$Ce_{0.8}Gd_{0.2}O_{1.9}$ (LSCF–CGO) thin film cathodes, Solid State Ion. 212 (2012) 10–17.
[26] B.F. Angoua, P.R. Cantwell, E.A. Stach, E.B. Slamovich, Crystallization and electrochemical performance of $La_{0.6}Sr_{0.4}Co_{0.2}Fe_{0.8}O_{3-\delta}$-$Ce_{0.8}Gd_{0.2}O_{1.9}$ thin film cathodes processed by single solution spray pyrolysis, Solid State Ion. 203 (2011) 62–68.
[27] J. Zamudio-García, L. Caizán-Juanarena, J.M. Porras-Vázquez, E.R. Losilla, D. Marrero-López, Unraveling the influence of the electrolyte on the polarization resistance of nanostructured $La_{0.6}Sr_{0.4}Co_{0.2}Fe_{0.8}O_{3-\delta}$ cathodes, Nanomaterials 12 (2022) 3936.
[28] A.F. Mohd Abd Fatah, A.Z. Rosli, A.A. Mohamad, A. Muchtar, T.U. Noh, N. A. Hamid, Structural characterization and performance optimization of LSCF–based mechanical physical composite cathodes for intermediate–temperature solid oxide fuel cells: a review, Mater. Today Commun. 41 (2024) 110597.
[29] H.G. Desta, G. Gebreslassie, J. Zhang, B. Lin, Y. Zheng, J. Zhang, Enhancing performance of lower-temperature solid oxide fuel cell cathodes through surface engineering, Prog. Mater. Sci. 147 (2025) 101353.
[30] D. Ding, X. Li, S.Y. Lai, K. Gerdes, M. Liu, Enhancing SOFC cathode performance by surface modification through infiltration, Energy Environ. Sci. 7 (2014) 552–575.
[31] S. Baratov, E. Filonova, A. Ivanova, M.B. Hanif, M. Irshad, M.Z. Khan, M. Motola, S. Rauf, D. Medvedev, Current and further trajectories in designing functional materials for solid oxide electrochemical cells: a review of other reviews, J. Energy Chem. 94 (2024) 302–331.
[32] L. dos Santos-Gómez, J. Zamudio-García, J.M. Porras-Vázquez, E.R. Losilla, D. Marrero-López, Recent progress in nanostructured electrodes for solid oxide fuel cells deposited by spray pyrolysis, J. Power Sources 507 (2021) 230277.

[33] X. Tong, C. Li, K. Xu, N. Wang, K. Brodersen, Z. Yang, M. Chen, Nanoengineering of electrodes via infiltration: an opportunity for developing large-area solid oxide fuel cells with high power density, Nanoscale 15 (2023) 16362–16370.

[34] N. Hedayat, Y. Du, H. Ilkhani, Review on fabrication techniques for porous electrodes of solid oxide fuel cells by sacrificial template methods, Renew. Sustain. Energy Rev. 77 (2017) 1221–1239.

[35] S. Mi, Z. Liu, C. Luo, L. Cai, Z. Zhang, L. Li, A review on preparing new energy ultrafine powder materials by freeze-drying, Dry. Technol. 38 (2020) 1544–1564.

[36] B. Amelo, 'Pert HighScore Plus, version 3.0 e, The Netherlands (2012).

[37] A.C. Larson, R.B.Von DreeleGsas, Report lAUR (1994) 86-748.

[38] T.H. Wan, M. Saccoccio, C. Chen, F. Ciucci, Influence of the discretization methods on the distribution of relaxation times deconvolution: implementing radial basis functions with DRTtools, Electrochim. Acta 184 (2015) 483–499.

[39] D. Johnson, ZView: a software program for IES analysis, version 2.8, Scribner Associates, Inc, Southern Pines, NC, 2002.

[40] O. Yamamoto, Y. Takeda, R. Kanno, M. Noda, Perovskite-type oxides as oxygen electrodes for high temperature oxide fuel cells, Solid State Ion. 22 (1987) 241–246.

[41] H. Yokokawa, Understanding materials compatibility, Annu. Rev. Mater. Res. 33 (2003) 581–610.

[42] L. dos Santos-Gómez, J. Hurtado, J.M. Porras-Vázquez, E.R. Losilla, D. Marrero-López, Durability and performance of CGO barriers and LSCF cathode deposited by spray-pyrolysis, J. Eur. Ceram. Soc. 38 (2018) 3518–3526.

[43] D. Pérez-Coll, D. Marrero-López, P. Núñez, S. Piñol, J. Frade, Grain boundary conductivity of $Ce_{0.8}Ln_{0.2}O_{2-\delta}$ ceramics (Ln= Y, La, Gd, Sm) with and without Co-doping, Electrochim. Acta 51 (2006) 6463–6469.

[44] L. dos Santos-Gómez, J. Zamudio-García, L. Caizán-Juanarena, J.M. Porras-Vázquez, D. Marrero-López, Design and optimization of self-assembled nanocomposite electrodes for SOFCs, J. Power Sources 613 (2024) 234866.

[45] Y. Sun, D. Jin, X. Zhang, Q. Shao, C. Guan, R. Li, F. Cheng, X. Lin, G. Xiao, J. Wang, Controllable technology for thermal expansion coefficient of commercial materials for solid oxide electrolytic cells, Materials 17 (2024) 1216.

[46] Q. Zhang, Y. Hou, L. Chen, L. Wang, K. Chou, Enhancement of electrochemical performance for proton conductive solid oxide fuel cell by 30%GDC-LSCF cathode, Ceram. Int. 48 (2022) 17816–17827.

[47] A.S. Painter, Y.-L. Huang, E.D. Wachsman, Durability of $(La_{0.8}Sr_{0.2})_{0.95}MnO_{3-\delta}$-$(Er_{0.2}Bi_{0.8})_2O_3$ composite cathodes for low temperature SOFCs, J. Power Sources 360 (2017) 391–398.

[48] L. Nie, M. Liu, Y. Zhang, M. Liu, $La_{0.6}Sr_{0.4}Co_{0.2}Fe_{0.8}O_{3-\delta}$ cathodes infiltrated with samarium-doped cerium oxide for solid oxide fuel cells, J. Power Sources 195 (2010) 4704–4708.

[49] L. Dos Santos-Gómez, J.M. Porras-Vázquez, E. Losilla, F. Martín, J.R. Ramos-Barrado, D. Marrero-López, Stability and performance of $La_{0.6}Sr_{0.4}Co_{0.2}Fe_{0.8}O_{3-\delta}$ nanostructured cathodes with Ce0. 8Gd0. 2O1. 9 surface coating, J. Power Sources 347 (2017) 178–185.

[50] L. Wu, J. Sun, H. Qi, B. Tu, C. Xiong, F. Chen, P. Qiu, Boosting steam tolerance and electrochemical performance of an $La_{0.6}Sr_{0.4}Co_{0.2}Fe_{0.8}O_{3-\delta}$-based air electrode for protonic ceramic electrochemical cells, J. Mater. Chem. A 12 (2024) 25979–25987.

[51] J. Lee, K. Ju, H.J. Yoo, S.E. Jo, H. Kim, G. Park, G. Han, W. Park, G.Y. Cho, H. J. Kim, J. An, A nanocrystalline $La_{0.6}Sr_{0.4}Co_{0.4}Fe_{0.6}O_{3-\delta}$ interlayer for an enhanced oxygen electrode–electrolyte interface in solid oxide cells, J. Mater. Chem. A 13 (2025) 14743–14750.

[52] J. Sar, L. Dessemond, E. Djurado, Electrochemical properties of graded and homogeneous $Ce_{0.9}Gd_{0.1}O_{2-\delta}$–$La_{0.6}Sr_{0.4}Co_{0.2}Fe_{0.8}O_{3-\delta}$ composite electrodes for intermediate-temperature solid oxide fuel cells, Int. J. Hydrog. Energy 41 (2016) 17037–17043.

[53] C. Gao, Y. Liu, K. Xi, S. Jiao, R. Tomov, R.V. Kumar, Improve the catalytic property of $La_{0.6}Sr_{0.4}Co_{0.2}Fe_{0.8}O_3$/$Ce_{0.9}Gd_{0.1}O_2$ (LSCF/CGO) cathodes with CuO nanoparticles infiltration, Electrochim. Acta 246 (2017) 148–155.

[54] D. Beckel, U.P. Muecke, T. Gyger, G. Florey, A. Infortuna, L.J. Gauckler, Electrochemical performance of LSCF based thin film cathodes prepared by spray pyrolysis, Solid State Ion. 178 (2007) 407–415.

[55] E. Zhao, X. Liu, L. Liu, H. Huo, Y. Xiong, Effect of $La_{0.8}Sr_{0.2}Co_{0.2}Fe_{0.8}O_{3-\delta}$ morphology on the performance of composite cathodes, Progress Natural Science Materials International 24 (2014) 24–30.

[56] C. Fu, K. Sun, N. Zhang, X. Chen, D. Zhou, Electrochemical characteristics of LSCF–SDC composite cathode for intermediate temperature SOFC, Electrochim. Acta 52 (2007) 4589–4594.

[57] M.R. Cesário, D.A. Macedo, A.E. Martinelli, R.M. Nascimento, B.S. Barros, D.M. A. Melo, Synthesis, structure and electrochemical performance of cobaltite-based composite cathodes for IT-SOFC, Cryst. Res. Technol. 47 (2012) 723–730.

[58] Z. Wang, H. Sun, J. Li, X. Guo, Q. Hu, Z. Yang, F. Yu, G. Li, Modified $La_{0.6}Sr_{0.4}Co_{0.2}Fe_{0.8}O_{3-\delta}$ cathodes with the infiltration of $Er_{0.4}Bi_{1.6}O_3$ for intermediate-temperature solid oxide fuel cells, Int. J. Hydrog. Energy 46 (2021) 22932–22941.

[59] G. Li, B. He, Y. Ling, J. Xu, L. Zhao, Highly active YSB infiltrated LSCF cathode for proton conducting solid oxide fuel cells, Int. J. Hydrog. Energy 40 (2015) 13576–13582.

[60] Y. Matsuzaki, I. Yasuda, Electrochemical properties of reduced-temperature SOFCs with mixed ionic–electronic conductors in electrodes and/or interlayers, Solid State Ion. 152-153 (2002) 463–468.

[61] Y. Yao, C. Wang, Y. Ma, H. Ye, Y. Liu, J. Liu, X. Zhao, T. Tao, Y. Yao, S. Lu, Preparation and performance of a nano-honeycomb cathode for microtubular solid oxide fuel cells, Int. J. Hydrog. Energy 48 (2023) 5229–5236.